Experimental characterization of a nonlinear mechanical oscillator with softening behaviour for large displacements

Nonlinear Dyn
https://doi.org/10.1007/s11071-024-09435-9

ORIGINAL PAPER

Experimental characterization of a nonlinear mechanical oscillator with softening behaviour for large displacements

D. Anastasio · S. Marchesiello · C. Svelto · G. Gatti

Received: 2 November 2023 / Accepted: 9 February 2024

Abstract This paper presents an experimental insight into the performance of a mechanical oscillator consisting of an X-shaped-spring configuration. This configuration achieves an overall softening characteristic with quasi-zero stiffness behaviour far away from the static equilibrium point. Such a geometrical nonlinear configuration has attracted significant research attention in the last few years, particularly for its application as a vibration isolator with the possibility to extend the quasi-zero-stiffness region beyond that of the classical three-spring nonlinear isolator. However, previous experimental evidence has been limited to small amplitude vibration excitation only. Furthermore, it has been focused mainly on the isolation region, rather than on the large amplitude response, thus circumventing an insight on the damping effects and its modelling. To address this gap, in this paper, both frequency sweeps and random excitations are applied to a prototype device for experimental characterization. A nonlinear stiffness model is developed based on the geometry of the system and a nonlinear damping model is assumed based on experimental observation. The proposed model accurately describes the dynamic behaviour of the system as shown by comparison of theoretical and experimental data.

Keywords Vibration control · Vibration isolation · Negative stiffness · Nonlinear damping · Nonlinear stiffness · Softening stiffness

1 Introduction

Nonlinear oscillators have received significant attention in recent decades to improve the performance of dynamical systems, particularly within the fields of vibration isolation [1], vibration energy harvesting [2], vibration absorption [3], shock isolation [4], and broader vibration control applications [5].

Traditionally, nonlinearity has been incorporated into mechanical systems by properly designing and customizing the stiffness of elastic suspensions through specific geometric configurations of springs and mechanisms. One typical application is the

Supplementary Information The online version contains supplementary material available at https://doi.org/10.1007/s11071-024-09435-9.

D. Anastasio (✉) · S. Marchesiello
Dipartimento di Ingegneria Meccanica ed Aerospaziale, Politecnico di Torino, Turin, Italy
e-mail: dario.anastasio@polito.it

C. Svelto
Dipartimento di Elettronica, Informazione e Bioingegneria, Politecnico di Milano, Milan, Italy

G. Gatti
Dipartimento di Ingegneria Meccanica, Energetica e Gestionale, Università della Calabria, Rende, Italy

Published online: 29 March 2024

inclusion of positive and negative stiffness elements in parallel to achieve geometrical nonlinear stiffness.

Diamond structures have been suggested for applications involving vibration isolation [6–8] and vibration absorption [9]. Scissor-like or X-shaped-link structures have been proposed for purposes such as vibration isolation [10–12], vibration absorption [13], vibration energy harvesting [2], and for the development of new metamaterials [14]. In efforts to improve vibration isolation performance, various combinations of linkages and springs have been explored [15, 16], drawing inspiration from biological sources like limbs [17–19], paws [20, 21], cockroaches [22], and biological systems in general [23, 24].

Nonlinear force–displacement curves have also been achieved by simply connecting linear springs arranged in a nonlinear geometric configuration. To this end, designs employing one pair [25], two pairs [26] and three pairs [27] of inclined springs have been proposed to expand the isolation capabilities. The configurations with one and two pairs of oblique springs have also proven effective in enhancing the performance of vibration energy harvesters, as discussed in [28] and [29].

The majority of the previously mentioned studies [6, 8, 10, 11, 15, 18–22, 24, 26, 27], primarily focused on achieving classical quasi-zero stiffness (QZS) force–deflection curves. This characteristic is valuable for simultaneously providing high-static and low-dynamic stiffness behaviour. It allows to carry a payload with a low static deformation while exhibiting a low natural frequency to enlarge the isolation region.

Other studies aimed to achieve a softening-hardening stiffness nonlinearity using one pair of asymmetrically inclined springs [30], a tri-stable nonlinear characteristic using two pairs of symmetric springs [29], softening-zero-hardening stiffness characteristics [31], sigmoidal-shaped force–displacement curves [32], and even tailored [33] and adjustable [34, 35] stiffness characteristics.

Modelling damping is of crucial importance in this kind of devices to predict a realistic dynamic behaviour. In some of the studies dealing with nonlinear oscillators exploiting combinations of linkages and springs, damping has been simply modelled as a translational linear viscous element [7–9, 19, 20, 36]. This assumption may hold when the amplitude of oscillation is relatively small, allowing for the consideration of an equivalent linear viscous damping term. In other studies, due to the presence of hinges in the coupling linkages, both translational and rotational linear viscous damping effects have been considered [6, 10–12, 15–17, 21–23], resulting in geometrical nonlinear damping effects along the translational motion direction.

In the most recent works focusing on nonlinear geometrical arrangement of linear spring pairs only, a linear viscous damping model has been considered [26–28]. However, the assumption that strongly nonlinear systems can be adequately represented by an equivalent linear viscous damper may be unrealistic when dealing with high-amplitude oscillations. Although viscous damping may result as a reasonable assumption in some cases [37, 38], dry friction can also manifest, especially when joints and mating linkages are adopted in a real prototype device.

Some attempts to model dry friction in nonlinear oscillators consisting of linkages and/or springs can be found in [39, 40], where models of nonlinear oscillators are presented with combination of viscous damping and dry friction. Recent experimental works on Coulomb friction effects on the response of a linear oscillator have been reported in [41, 42].

Recent investigations into nonlinear oscillators employing pairs of inclined springs have not fully considered dry friction in their models. This paper thus contributes to advance the knowledge on the performance of nonlinear mechanical oscillators subject to large amplitude oscillations, where both strongly nonlinear stiffness and damping must be accounted for modelling. To validate the proposed model, a prototype device was constructed and tested experimentally, resulting in very-good agreement of the measured data with the theoretical prediction of the model.

Potential applications are foreseen in vibration energy harvesters, vibration isolators, and vibration absorbers, where having a softening elastic behaviour under large displacements may be of interest.

2 Modelling

2.1 System description, geometry, and static analysis

The system considered in this work is a X-shaped mechanical oscillator. A photo of the prototype device and its virtual model are shown in Fig. 1a and b respectively. Depending on its design parameters, this system can achieve a variety of elastic behaviours, encompassing linear, hardening, softening and QZS characteristics [35, 43]. This paper introduces a design approach that incorporates two symmetrical QZS regions, thereby achieving a softening behaviour under large-amplitude oscillations—the central objective of this work. Figure 1c and d, show the geometrical model of the device in its static equilibrium configuration and in an arbitrary displaced configuration, respectively. Four equal oblique springs with free length h_0 and stiffness k are connected between an oscillating mass, m, and a support structure. A one-degree-of-freedom underlying mechanism is adopted to constrain the oscillating mass relative displacement, z, along the horizontal direction. The underlying mechanism consists of one fixed bar constraining the oscillating mass motion to the horizontal direction only, and four oscillating bars used to guide spring compression and limit spring buckling. These elements are labelled in Fig. 1a. Revolute and translational joints are adopted to assemble the bars to the oscillating mass and the supporting structure. It is worth noticing that the prototype device in Fig. 1a employs two compression springs for each bar, to ensure proper operation throughout the entire range of motion of the sliding mass. Practically, the outer springs come into place when the inner ones are no longer under compression. In contrast, the schematic representation only shows one spring per bar, working both under compression and tension.

Due to symmetry, in the static equilibrium configuration for $z = 0$, which is shaded in Fig. 1b, each of the springs has the same assembled length, h, and the same distance, l_0, also holds between the centres of the rotational joints for each spring assembly. The parameters a and b define the springs inclination in the static equilibrium configuration.

When the oscillating mass moves, each pair of springs behaves differently. Figure 1b, shows the case when the mass moves in the positive direction, i.e. $z > 0$, so that spring pair on the right assumes length $h_1 < h_0$, while the pin-pin distance assumes length $l_1 < l_0$. Conversely, the spring pair on the left assumes length $h_2 > h_0$, while the pin-pin distance assumes length $l_2 > l_0$.

The following relations hold for the model in Fig. 1

$$\begin{aligned} l_1 &= \sqrt{(a-z)^2+b^2} \\ l_2 &= \sqrt{(a+z)^2+b^2} \\ h_1 &= h - l_0 + l_1 \\ h_2 &= h - l_0 + l_2 \\ l_0 &= \sqrt{a^2+b^2} \end{aligned} \qquad (1a-e)$$

The expression of the elastic force, f_e, as a function of the mass relative displacement, z, can be determined by considering the parallel contribution of the spring pair on the left and on the right, which yields

$$f_e = -2k\frac{(h_1-h_0)(a-z)}{l_1} + 2k\frac{(h_2-h_0)(a+z)}{l_2} \qquad (2)$$

So that, substituting Eq. (1a–e) in Eq. (2) gives

$$\begin{aligned} f_e = -2k\Bigg[& \frac{a-z}{\sqrt{(a-z)^2+b^2}} \\ & \left(h(1-\sigma) - \sqrt{a^2+b^2} + \sqrt{(a-z)^2+b^2}\right) \\ & - \frac{a+z}{\sqrt{(a+z)^2+b^2}}\left(h(1-\sigma) - \sqrt{a^2+b^2} + \sqrt{(a+z)^2+b^2}\right)\Bigg] \end{aligned} \qquad (3)$$

where the spring length factor, $\sigma = h_0/h$, is introduced, and represents the ratio of the free length of each spring to its assembled length in the static equilibrium configuration.

Depending on the different parameters in Eq. (3), very different behaviours can be realised, in terms of stiffness curve. Linear, hardening, softening, and quasi-zero stiffness characteristics can be achieved. The reader is directed to [43] for an insight.

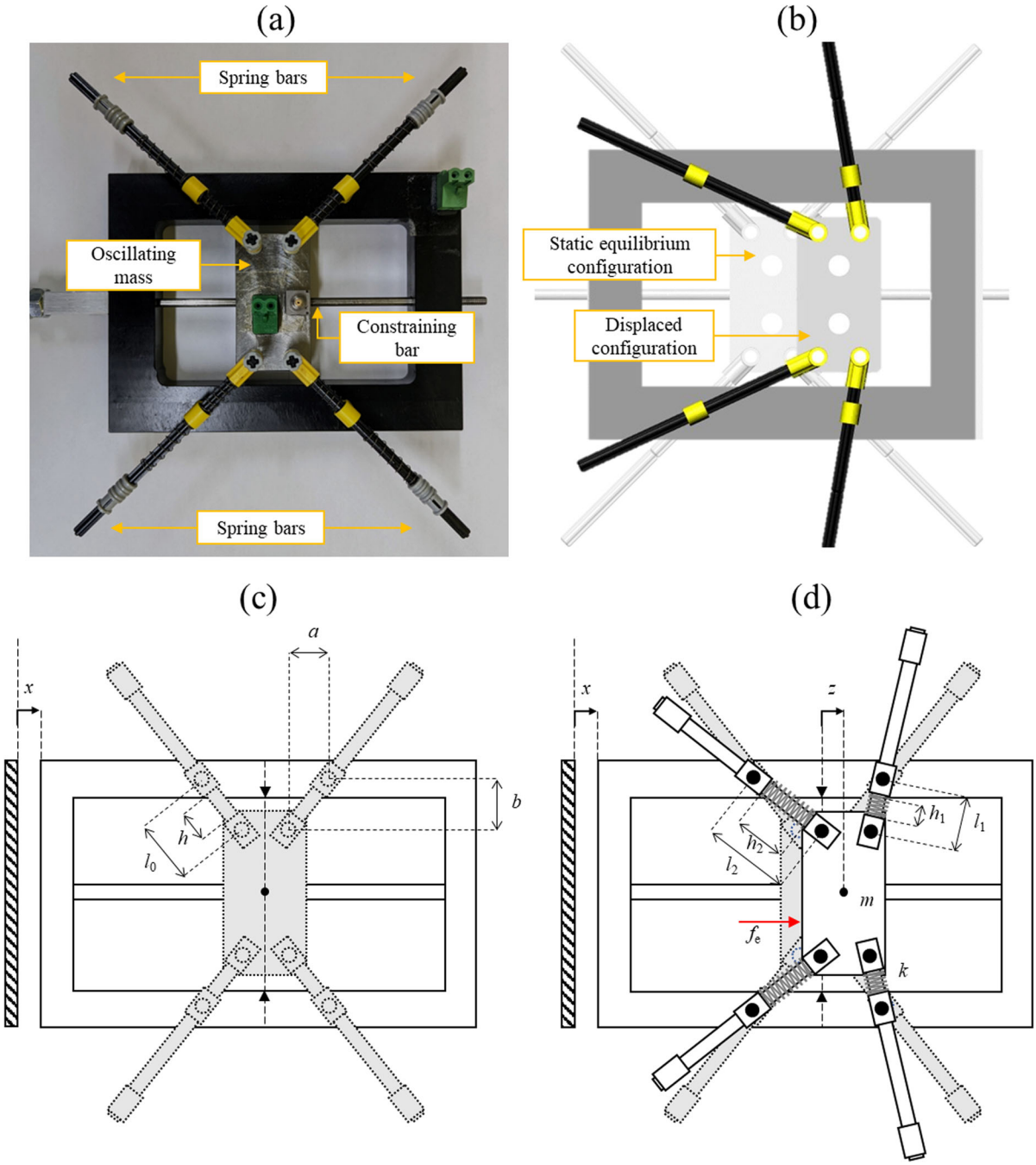

Fig. 1 X-shaped-spring system under study. Photo of the prototype device in **a**. Virtual model in **b** in equilibrium configuration (shaded) and in displaced configuration. Geometrical model in the static equilibrium configuration in **c**, and in an arbitrary displaced configuration in **d**

2.2 Tailoring the force–displacement curve to a sigmoidal characteristic

Among the different shapes of force–deflection characteristics achievable with the spring configuration shown in Fig. 1, the interest of this work is towards a shape of the force–displacement characteristic with positive stiffness at the static equilibrium configuration and two symmetric QZS regions at larger displacements, thus resembling a sigmoidal characteristic. This is achieved by solving both the first and second derivative of Eq. (3) (with respect to the relative displacement z) set to zero in terms of z and b. To limit the number of design parameters, it is conveniently assumed that $a = b$, and numerical simulations are run for different combinations of h_0 and h, which satisfy the mechanical implementation and geometry of the structure. A suitable theoretical solution gives the values of parameters listed in the first row of Table 1. Note that $|z_{ZS}|$ in Table 1, denotes the value of displacement at which a theoretical zero-stiffness is achieved. Comparing the theoretical solution for the spring parameters with a commercial spring catalogue, it was possible to select the actual values of parameters used for the prototype device, which are listed in the second row of Table 1. Note that in this case there is no value for $|z_{ZS}|$, as a true theoretical zero-stiffness point is missing due to the adoption of commercial springs with slightly different parameter values than those mathematically required.

Figure 2a shows the theoretical characteristic with zero-stiffness points and the actual characteristic due to the adopted commercial springs. Figure 2b represents the device configuration (i.e., the oscillating mass displacement) corresponding to the static characteristic in Fig. 2a.

2.3 Lagrange modelling and effect of variable inertia

The equation of motion of the system is determined using a Lagrange approach [44] and considering all the major moving components of the oscillator, i.e., the oscillating mass and the spring bars, which incline as the oscillating mass moves. Note that the oscillator is mounted so that it oscillates in the horizontal direction, thus the effect of gravity is neglected.

The kinetic energy of the system is obtained by considering the movements of the oscillating mass and of the four spring bars. The former is described by the variable z, while the latter is a combination of the displacement ΔG_j of the centre of mass G_j and the rotation γ_j of each bar ($j = 1, \ldots, 4$). The motion x imposed to the frame in Fig. 1c,d is set to zero in this section. The initial angle of each bar is denoted as γ_{j0} and refers to the equilibrium position. The following initial angles are set in this work: $\gamma_{10} = \gamma_{40} = 45°$ and $\gamma_{20} = \gamma_{30} = 135°$. A scheme of the motion of the first spring bar is depicted in Fig. 3 as an example (see Fig. 2b for the spring bars order).

The angle γ_1 can be easily obtained from the following trigonometric relation

$$\gamma_1 = \tan^{-1}\frac{b\tan\gamma_{10}}{b - z\tan\gamma_{10}} - \gamma_{10} \tag{4}$$

while the displacement ΔG_1 can be calculated by applying the cosine rule to the triangle G_1AG_1' in Fig. 3 and assuming that the position of the centre of mass of the bar is known. The expressions of the kinetic energy T and of the potential energy V read:

$$\begin{aligned} T &= T_{\mathrm{m}} + \sum_{j=1}^{4} T_{\mathrm{G_j}} + \sum_{j=1}^{4} T_{\gamma_{\mathrm{j}}} \\ &= \frac{1}{2}m\dot{z}^2 + \frac{1}{2}m_b\sum_{j=1}^{4}\dot{\Delta}_{G_j}^2 + \frac{1}{2}I_b\sum_{j=1}^{4}\dot{\gamma}_j^2 \end{aligned} \tag{5a}$$

$$V = \frac{1}{2}k\sum_{j=1}^{4}\left(h_j - h_0\right)^2 \tag{5b}$$

where m_b and I_b are the mass and the moment of inertia of a single spring bar. The effect of variable inertia is studied by applying a constant-rate variation of the relative displacement z from -0.03 m to $+0.03$ m and considering the system nominal characteristics listed in Table 1. The values of γ and ΔG for the four spring bars are plotted in Fig. 4.

Table 1 Nominal parameters

	a [m]	b [m]	$\lvert z_{ZS}\rvert$ [m]	h [m]	h_0 [m]	σ [1]	l_0 [m]	k [N/m]
Theoretical solution	0.0214	0.0214	0.0206	0.0164	0.0254	1.545	0.0303	250
Practical solution	0.0214	0.0214	–	0.0143	0.0254	1.7794	0.0303	250

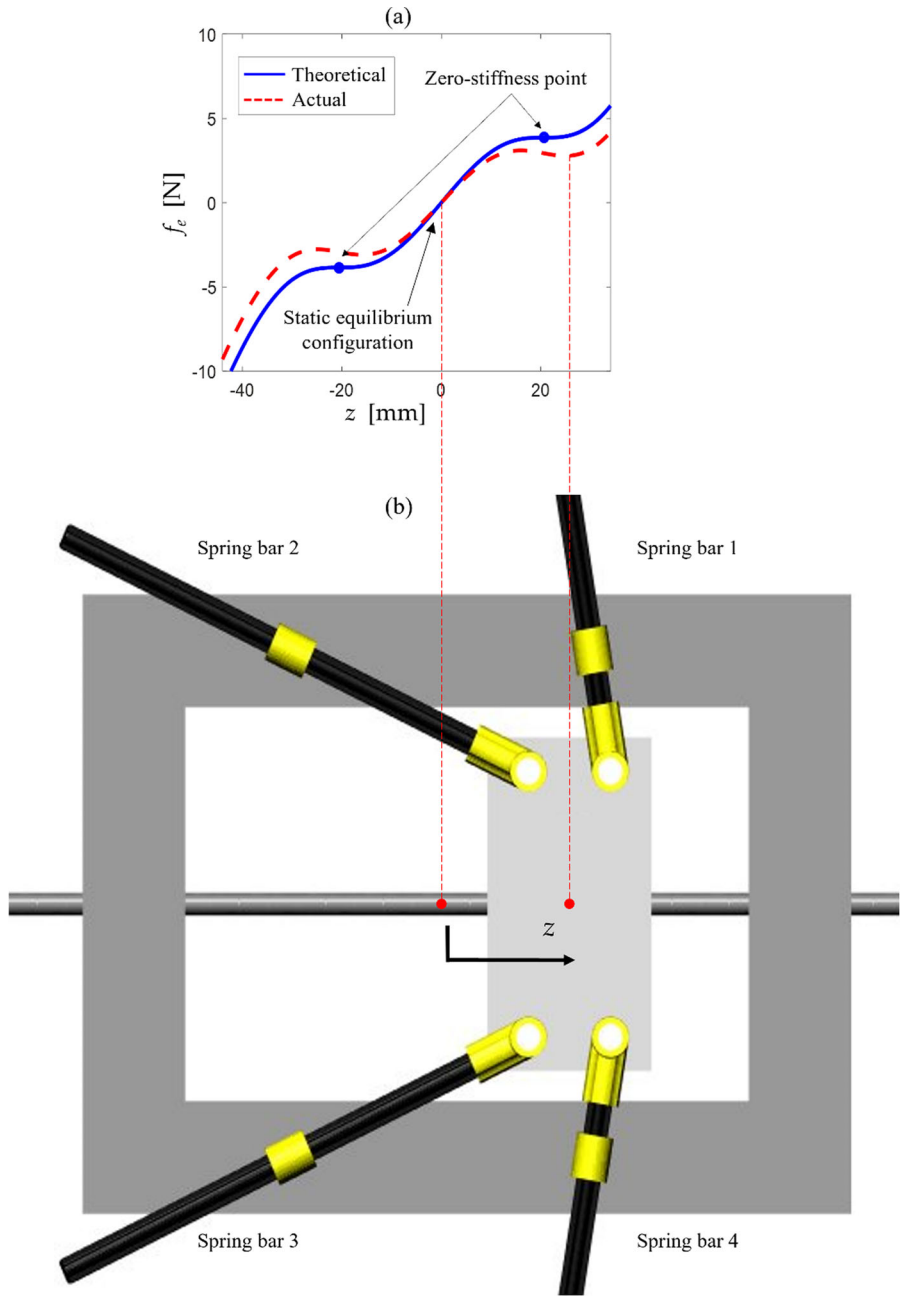

Fig. 2 **a** Sigmoidal characteristic of the force–deflection curve. **b** Configuration of the device corresponding to the QZS region in **a**

The percentage contributions of the single components to the kinetic energy T of the system (Eq. 5a) are depicted in Fig. 5 as a function of z. The component T_{m} associated with the movement of the mass m accounts for approximately 96% of the total kinetic energy of the system. Thus, it is a reasonable approximation to neglect the contributions from the other components in the dynamic model adopted in the following sections.

It has been verified both numerically and analytically that the derivative of the potential energy of Eq. (5b) with respect to the displacement variable z gives exactly the elastic force of Eq. (2).

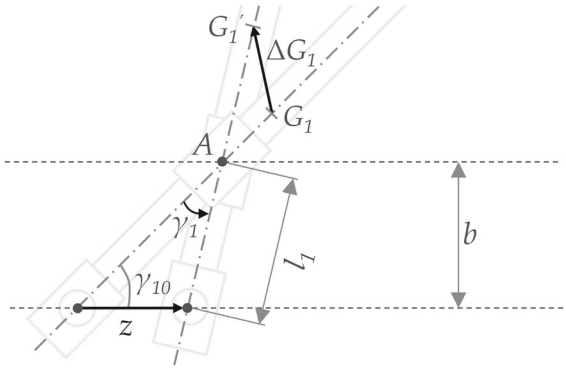

Fig. 3 Motion of the centre of mass of spring bar 1

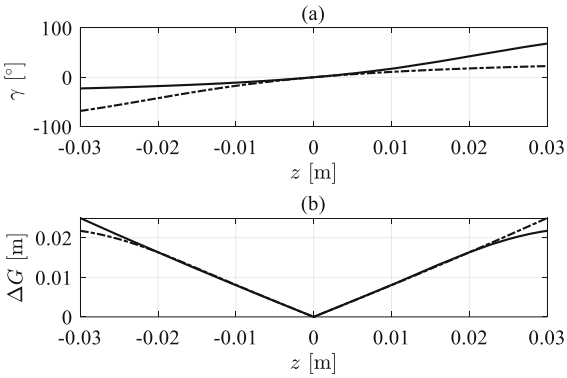

Fig. 4 Angle γ in **a** and displacement ΔG in **b** as a function of the relative displacement z. Continuous lines: spring bars 1, 4; dashed-dotted lines: spring bars 2, 3

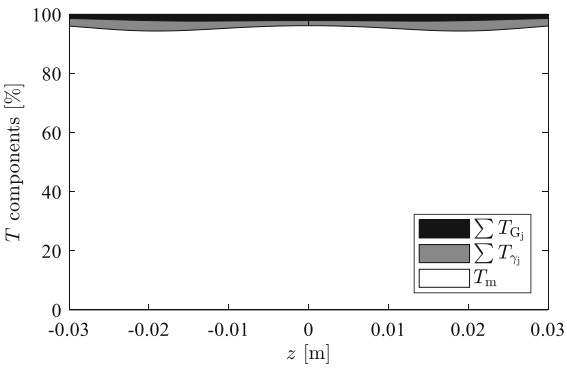

Fig. 5 Percentage components of the kinetic energy of the system

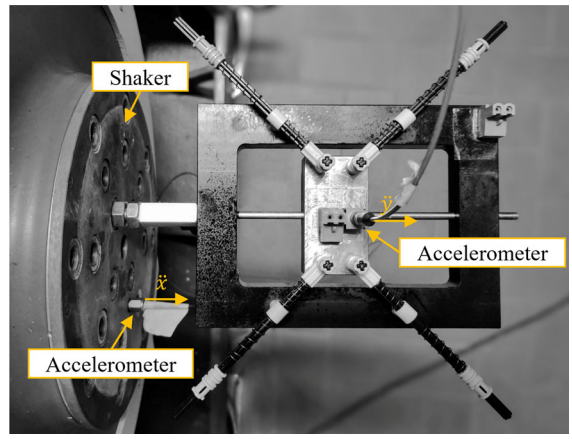

Fig. 6 Photo of the experimental assembly

3 Experimental work

3.1 Prototype assembly

The device is excited with an electromagnetic shaker (TIRA TV56280/LS-180) that exerts an acceleration $\ddot{x}$ to the frame. Two monoaxial accelerometers (B&K 4507-B004) are used to measure the acceleration of the shaker and the absolute acceleration of the oscillating mass, $\ddot{y}$. A photo of the experimental assembly is shown in Fig. 6 and a video showing the prototype in operating conditions is available in Online Appendix A.

The relative acceleration of the moving mass is described by the variable $\ddot{z} = \ddot{y} - \ddot{x}$, and the equation of motion therefore reads:

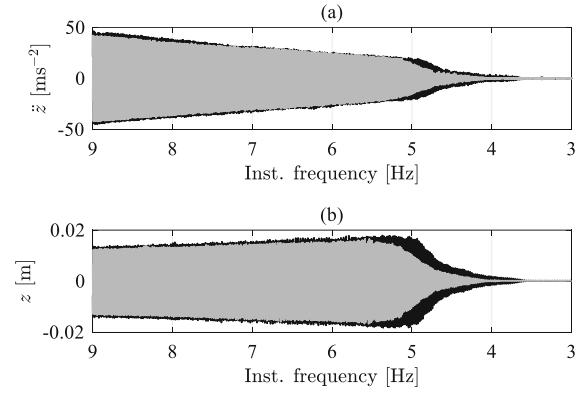

Fig. 7 Sweep tests. **a** Relative acceleration. **b** Relative displacement. Black line: base amplitude of 10 mm. Grey line: base amplitude of 9 mm

$$m\ddot{z} + f_e(z) + f_d(z, \dot{z}) = -m\ddot{x} \tag{6}$$

where $f_e(z)$ is the elastic force and $f_d(z, \dot{z})$ is the damping force. The latter is written as a function of both displacement z and velocity $\dot{z}$, and it will be derived from the experimental observations in the following sections. Note that the inertia term contains only the contribution of the moving mass, as already discussed in Sect. 2.3.

3.2 Sweep tests and restoring force surface

Two different frequency sweep tests are conducted with a linear rate of 0.1 Hz/s, from 9 down to 3 Hz (sweep-down) and with a sampling frequency of 512 Hz, using two amplitude values. The base amplitude of oscillations is controlled using LMS TestLab^{TM} software and it is set to 10 mm for the first test and 9 mm for the second. These values have been selected to induce large displacements in the system response without causing impacts or reaching physical constraints. The measured relative acceleration $\ddot{z}$ is plotted in Fig. 7a for both tests as a function of the instantaneous frequency of the input signal. The relative displacement z is obtained by double-integration of the corresponding acceleration signal $\ddot{z}$ and it is depicted in Fig. 7b for both tests. Notice that the maximum measured displacement in Fig. 7b is very close to the characteristic dimensions a and b of the device, as reported in Table 1.

From the measurements, it is observed how the system response rapidly decreases around 5 Hz, which is consistent with the softening behaviour that is expected from the design specifications of device.

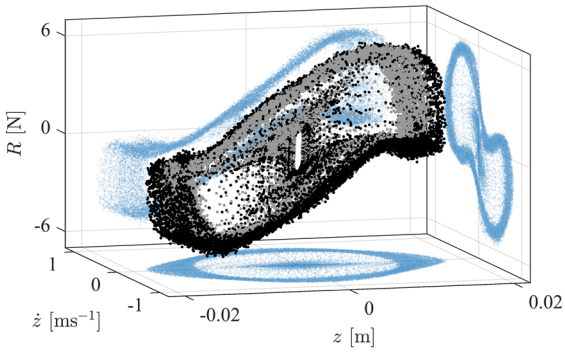

Fig. 8 Experimental restoring force surface. Black dots: base amplitude of 10 mm. Grey dots: base amplitude of 9 mm. Projections to side walls are in blue

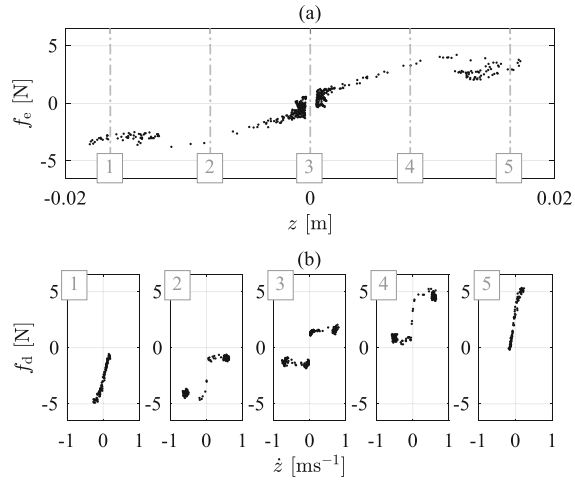

Fig. 9 **a** Experimental elastic force. **b** Experimental damping force across five different positions of the moving mass (− 16 mm, − 8 mm, 0 mm, + 8 mm, + 16 mm)

The restoring force R [45] of the system is defined as

$$R = f_e(z) + f_d(z, \dot{z}) = -m(\ddot{x} + \ddot{z}) = -m\ddot{y} \tag{7}$$

The experimental restoring force surface is denoted with $\widetilde{R}$ and is depicted in Fig. 8 as a function of displacement and velocity, considering both tests.

The Restoring Force Surface (RFS) method [45] is applied to obtain an estimate of the elastic and damping forces. In particular, an approximation of the elastic force can be visualised by slicing the restoring surface in the range of zero velocity, such that $|\dot{z}| < \epsilon_v$ with ϵ_v user-selected tolerance. The result is depicted in Fig. 9a with ϵ_v set to be 0.5% of $\max|\dot{z}|$. The softening behaviour of the elastic force, as specified in Fig. 2a from the theory, is also observed in Fig. 9a from the experiments, confirming the expectations.

A similar approach is adopted for the damping force. However, in this case the restoring surface is sliced in the neighbourhood of several positions z_k to track the possible evolution of the damping force along the movement of the oscillating mass. The results are shown in Fig. 9b considering five equally spaced positions such that $|z - z_k| < \epsilon_d, k = 1, \ldots, 5$ and ϵ_d set to be 0.5% of $\max|z|$.

The sliding friction behaviour is generally observed in Fig. 9b, as expected, but with two considerations:

1. The amplitude of the damping force is not constant with respect to the position of the moving mass. This can be explained by a non-constant normal force acting along z due to the interaction of the spring bars. A similar behaviour has been previously observed in [40, 46] due to the effect of the two rods on a constraining bar. An accurate damping model of the considered system should therefore account for the position-dependent nature of the friction force.
2. There exists a region of viscous-type behaviour for small velocities. This can be clearly observed in Fig. 9b. This effect can be incorporated into the damping model by introducing a transition from viscous (small velocities) to frictional behaviour, for instance by employing a hyperbolic tangent function [48].

A damping model that takes into account these two observations is therefore considered in the following section.

3.3 Fitting model to experiment

The experimental restoring force $\widetilde{R}$ is fitted to the model in Eq. (7), which is the sum of the elastic force in Eq. (3) and of a proper damping force $f_\mathrm{d}(z,\dot{z})$. In a previous work [47] using the same prototype device, a simple damping model was adopted. Based on the new experimental evidence observed in the previous section, the damping model proposed in this paper is extended as follows:

$$\begin{aligned} f_\mathrm{d}(z,\dot{z}) &= \mu(z)\tanh\left(\frac{4\dot{z}}{v_\mathrm{t}(z)}\right) \\ &= \left[\mu_0 + \tanh\left(\mu_1 z + \mu_2 z^2\right)\right]\tanh\left(\frac{4\dot{z}}{\alpha+\beta z^2}\right) \end{aligned} \tag{8}$$

Equation (8) is based on the continuous-velocity friction model [48] with both amplitude and viscous-region functions of the relative displacement z. The amplitude $\mu(z)$ is expressed as the sum of a constant term μ_0 (in [N]) and a hyperbolic tangent function, whose argument contains a quadratic function of the relative displacement. The first-order term $\mu_1 z$ accounts for possible asymmetries in the damping force. The use of the hyperbolic tangent function is to saturate the force amplitude in case of model extrapolation outside the training data set, to make sure that the system response does not diverge or become unstable [49]. The viscous-transition region is ruled by the velocity term $v_\mathrm{t}(z) = \alpha + \beta z^2$ that is a quadratic function of z with coefficients α (in [m/s]) and β (in [1/(m·s)]). Note that $\beta = 0$ returns a constant transition velocity as in [48]. The whole damping model captures therefore the amplitude-dependent sliding friction behaviour with viscous-like transition at small velocities, relying on five parameters $(\mu_0, \mu_1, \mu_2, \alpha, \beta)$. It does not consider other known frictional phenomena such as time-lag, microslip, or dwell-time dependence [50], which generally require more sophisticated modelling approaches and dedicated experimental investigations beyond the scope of this study.

As for the elastic model, the practical solution values of Table 1 are considered as initial guesses. Only the stiffness k and the initial spring length h_0 are included in the optimisation problem, since the other dimensional parameters have been accurately measured before the experimental tests.

The following nonlinear least-squares minimisation problem is therefore set:

$$\widehat{\boldsymbol{\theta}} = \mathrm{argmin}_{\boldsymbol{\theta}} \left|\left|\widetilde{R} - R(\boldsymbol{\theta})\right|\right|^2 \text{ subject to } \boldsymbol{l} \le \boldsymbol{\theta} \le \boldsymbol{u} \tag{9}$$

where $\boldsymbol{\theta} = [k, h_0, \mu_0, \mu_1, \mu_2, \alpha, \beta]^\mathrm{T}$ is the vector of parameters to be optimized, with $\boldsymbol{l}$ and $\boldsymbol{u}$ being the lower and upper constraints, respectively. The necessity of a constrained optimisation problem arises from the need of obtaining a feasible solution in the space of parameter dimensions. The trust-region method [51] is adopted to solve the minimisation problem of Eq. (9), and the result over the iterations is depicted in Fig. 10.

Optimised parameters are listed below in Table 2 and compared to the initial guess corresponding to the nominal parameters. Note that the damping terms are all initially set to zero.

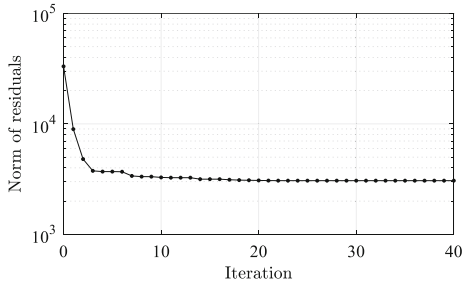

Fig. 10 Norm of the residuals over the iterations (logarithmic scale)

Table 2 Optimised parameters

	k [Nm^{-1}]	h_0 [m]	μ_0 [N]	μ_1 [Nm^{-1}]	$10^3\mu_2$ [Nm^{-2}]	α [ms^{-1}]	$10^3\beta$ [1/(ms)]
Initial value	250	0.026	0	0	0	0	0
Range	200 ÷ 400	0.022 ÷ 0.030	0 ÷ 5	− 50 ÷ 50	0 ÷ 10	0 ÷ 1	0 ÷ 5
Final value	308	0.028	1.60	25.31	3.35	0.08	1.17

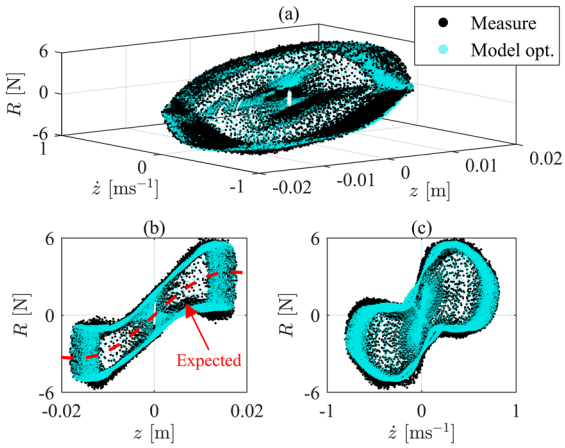

Fig. 11 Experimental (black) and modelled (cyan) restoring force surface. **a** 3D visualisation. **b** Force–displacement plot with expected behaviour in dashed red line. **c** Force–velocity plot

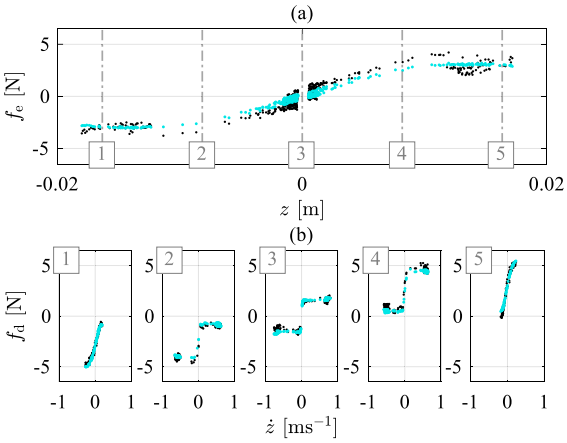

Fig. 12 **a** Experimental (black) and modelled (cyan) elastic force. **b** Experimental (black) and modelled (cyan) damping force across five different positions of the moving mass (− 16 mm, − 8 mm, 0 mm, + 8 mm, + 16 mm)

The modelled restoring force R and the experimental one $\widetilde{R}$ are plotted in Fig. 11 w.r.t. displacement and velocity.

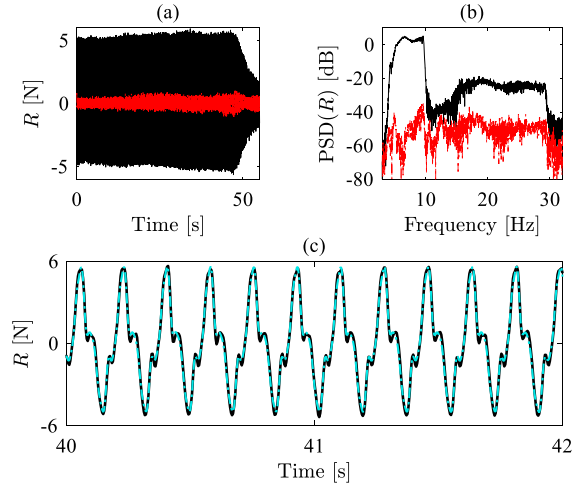

Fig. 13 Restoring force in the time domain in **a** and **c**, and in the frequency domain in **b**. Black line: experimental data. Dashed-dotted red line in **a** and **b**: model residual. Dashed-dotted cyan line in **c**: model output

A more detailed representation is proposed in Fig. 12, recalling the plots of Fig. 9. Figure 12a shows the experimental (black) and modelled (cyan) elastic forces, while Fig. 12b shows the experimental (black) and modelled (cyan) damping forces at the same five positions shown in Fig. 9.

The residual $\epsilon = \widetilde{R} - R$ is plotted in Fig. 13a-b in time and frequency (PSD) domains. The proposed model well captures the system behaviour, with a low residual error. This is particularly evident in the frequency region of the excitation (i.e., [3 ÷ 9] Hz), where the residual lies around 60 dB below the signal. This is considered a satisfactory outcome, given the manufacturing and assembling tolerances of the device. The accuracy of the model can be visualised in Fig. 13c, with a two-second zoomed view of the experimental (black) and modelled (dashed-dotted cyan) restoring forces: the two curves visually overlap.

To inspect the sensitivity of the damping force to its parameters, a deeper investigation is proposed in Fig. 14, where the parameters $\mu_0, \mu_1, \mu_2, \alpha, \beta$ are

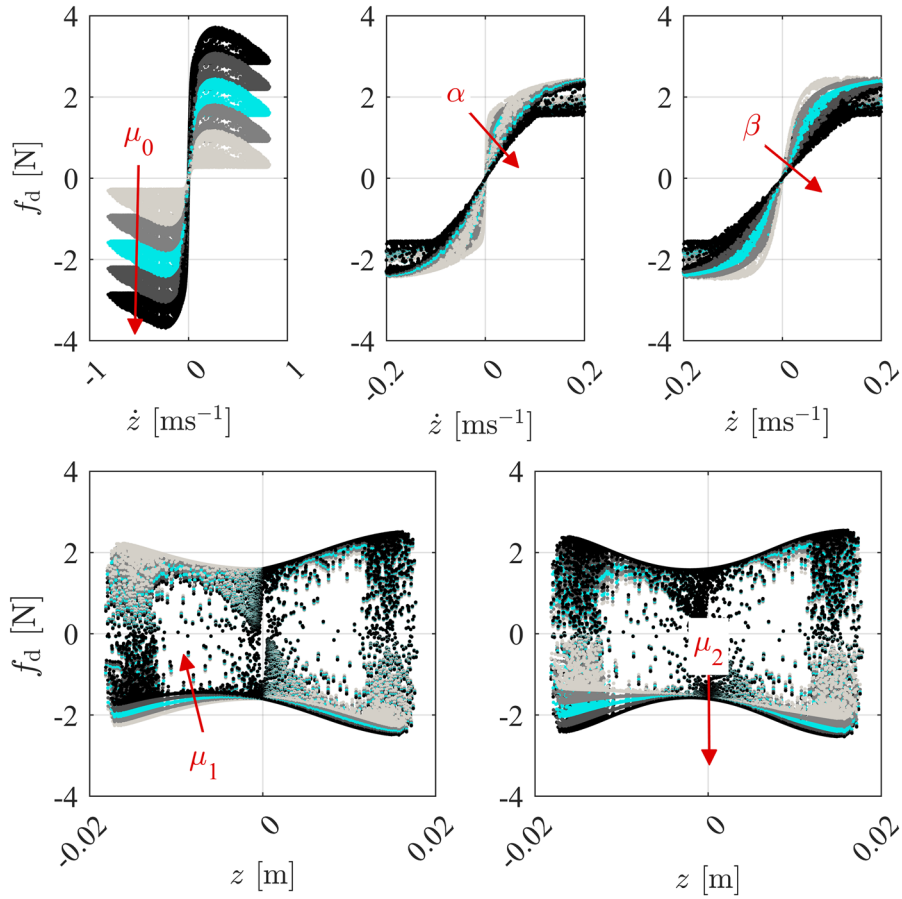

Fig. 14 Effect of parameters on the damping force. Cyan colour indicates the optimised parameters

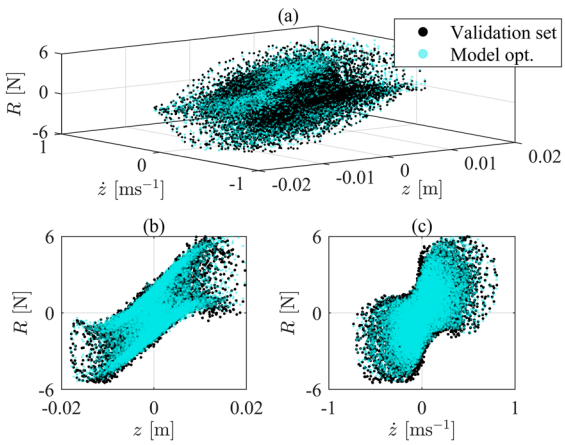

Fig. 15 Experimental (black) and modelled (cyan) restoring force surface of the validation set. **a** 3D visualisation. **b** Force–displacement plot. **c** Force–velocity plot

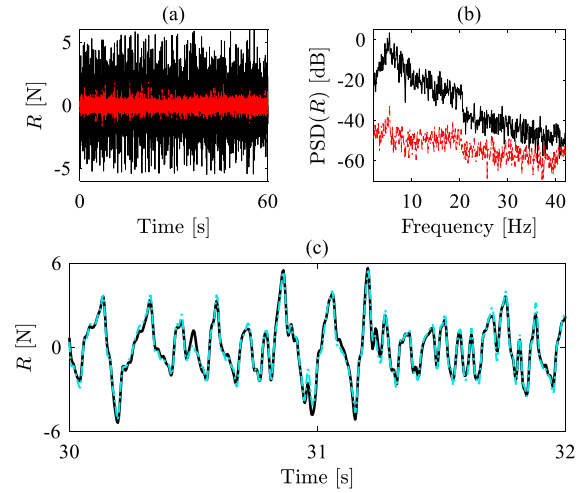

Fig. 16 Restoring force of the validation set in the time domain in **a** and **c**, and in the frequency domain in **b**. Black line: experimental data. Dashed-dotted red line in **a** and **b**: model residual. Dashed-dotted cyan line in **c**: model output

considered as [0.2, 0.6, 1, 1.4, 1.8] times of their final values in Table 2. As expected, the amplitude μ_0 has the greatest impact on the damping force. The parameters α and β of viscous-transition region are instead the least sensitive to variations in affecting the model of the restoring force, and their effect is mainly localised around the zero-velocity region. Nevertheless, they ensure that the low-velocity behaviour is appropriately captured by the damping model.

3.4 Validation with random test

The optimised model is validated on a second data set with a broadband random excitation in the frequency range [2 ÷ 20] Hz. The same experimental setup of Sect. 3.1 is used, with a sampling frequency of 512 Hz and data recorded for 60 s. The base amplitude of oscillations in this case is 7 mm RMS. The experimental restoring force and the model estimation are visualised in Fig. 15, while the residual is plotted in Fig. 16a and b in time and frequency (PSD) domains, respectively. The system dynamics are successfully captured also in this case, with the model residual being an average of 48 dB lower than the signal in the frequency range of the excitation. A two-second zoomed view of the experimental (black) and modelled (dashed-dotted cyan) restoring forces is also depicted in Fig. 16c to visualise the model's prediction accuracy. The two curves well overlap also in this case.

4 Conclusions

This work has investigated the static and dynamic characteristics of a nonlinear suspension with two pairs of inclined linear springs arranged in an X-shaped configuration. A relationship among the system parameters has been found resulting in a softening force–displacement characteristic, with two symmetric quasi-zero stiffness points far away from the static equilibrium configuration. Such a relation results in the free length of the springs being linked to their assembled length.

A prototype device was built and tested for experimental validation of the theoretical model. Frequency sweep excitations were used to collect data and the Restoring Force Surface method was used to identify the best estimate of the system parameters to fit the experimental data. A second set of experimental data, with a broadband excitation, was used to validate the model. The final residuals of the testing and validation sets were approximately 60 dB and 48 dB lower than the measurements, respectively. This is considered to be very satisfactory, given the relatively large tolerances in manufacturing and assembling the prototype device. Dry-friction and viscous-damping models were adopted, and the theoretical force–displacement characteristic was inferred from the geometric configuration of the device.

Other dynamic models proposed in the recent literature for this class of X-shaped-spring oscillators rely on a linear viscous damping model for small displacement. The work presented in this paper shows that a more complex damping model is needed to fit experimental results for large amplitude motion. In the experiments, the oscillating mass of the proposed oscillator moved up to an amplitude of about 18 mm both in frequency sweep and random tests. This is comparable with the characteristic dimension of the device, which is about 2 cm, and thus represents a relatively large motion.

This paper advances the knowledge on the characteristics of X-shaped-spring nonlinear elastic suspensions with softening characteristics and for large displacement range. From a practical engineering point of view, potential applications of the device are foreseen in the field of vibration isolation, vibration absorption, and vibration energy harvesting.

Funding This research received no specific grant from any funding agency in the public, commercial, or not-for-profit sectors.

Data availability The datasets generated and/or analysed during the current study are not publicly available but they are available from the corresponding author upon reasonable request.

Declarations

Conflict of interest The authors have not disclosed any competing interests.

References

1. Ibrahim, R.A.: Recent advances in nonlinear passive vibration isolators. J. Sound Vib. **314**(3–5), 371–452 (2008). https://doi.org/10.1016/j.jsv.2008.01.014
2. Li, M., Zhou, J., Jing, X.: Improving low-frequency piezoelectric energy harvesting performance with novel X-structured harvesters. Nonlinear Dyn. **94**, 1409–1428 (2018). https://doi.org/10.1007/s11071-018-4432-6
3. Ding, H., Chen, L.-Q.: Designs, analysis, and applications of nonlinear energy sinks. Nonlinear Dyn. **100**, 3061–3107 (2020). https://doi.org/10.1007/s11071-020-05724-1
4. Ledezma-Ramírez, D.F., Tapia-Gonzalez, P.E., Ferguson, N., Brennan, M.J., Tang, B.: Recent advances in shock isolation: An overview and future possibilities. Appl. Mech. Rev. **71**, 060802 (2019). https://doi.org/10.1115/1.4044190
5. Lu, Z., Wang, Z., Zhou, Y., Lu, X.: Nonlinear dissipative devices in structural vibration control: a review. J. Sound Vib. **423**, 18–49 (2018). https://doi.org/10.1016/j.jsv.2018.02.052
6. Chong, X., Wu, Z., Li, F.: Vibration isolation properties of the nonlinear X-combined structure with a high-static and low-dynamic stiffness: theory and experiment. Mech. Syst. Signal Process. **179**, 109352 (2022). https://doi.org/10.1016/j.ymssp.2022.109352
7. Yu, Y., Yao, G., Wu, Z.: Nonlinear primary responses of a bilateral supported X-shape vibration reduction structure. Mech. Syst. Signal Process. **140**, 106679 (2020). https://doi.org/10.1016/j.ymssp.2020.106679
8. Xiong, Y., Li, F., Wang, Yu.: A nonlinear quasi-zero-stiffness vibration isolation system with additional X-shaped structure: theory and experiment. Mech. Syst. Signal Process. **177**, 109208 (2022). https://doi.org/10.1016/j.ymssp.2022.109208
9. Xiong, X., Wang, Y., Li, J., Li, F.: Internal resonance analysis of bio-inspired X-shaped structure with nonlinear vibration absorber. Mech. Syst. Signal Process. **185**, 109809 (2023). https://doi.org/10.1016/j.ymssp.2022.109809
10. Bian, J., Jing, X.: Analysis and design of a novel and compact X-structured vibration isolation mount (X-Mount) with wider quasi-zero stiffness range. Nonlinear Dyn. **101**, 2195–2222 (2020). https://doi.org/10.1007/s11071-020-05878-y
11. Chai, Y., Jing, X., Chao, X.: X-shaped mechanism based enhanced tunable QZS property for passive vibration isolation. Int. J. Mech. Sci. **218**, 107077 (2022). https://doi.org/10.1016/j.ijmecsci.2022.107077
12. Jing, X., Zhang, L., Jiang, G., Feng, X., Guo, Y., Xu, Z.: Critical factors in designing a class of X-shaped structures for vibration isolation. Eng. Struct. **199**, 109659 (2019). https://doi.org/10.1016/j.engstruct.2019.109659
13. Bian, J., Jing, X.: A nonlinear X-shaped structure based tuned mass damper with multi-variable optimization (X-absorber). Commun. Nonlinear Sci. Numer. Simulat. **99**, 105829 (2021). https://doi.org/10.1016/j.cnsns.2021.105829
14. Li, Y., Li, H., Liu, X., Yan, S.: Bandgap and wave propagation of spring–mass–truss elastic metamaterial with a scissor-like structure. J. Phys. D Appl. Phys. **55**, 055303 (2022). https://doi.org/10.1088/1361-6463/ac2fd7
15. Yan, G., Zou, H.-X., Wang, S., Zhao, L.-C., Gao, Q.-H., Tan, T., Zhang, W.-M.: Large stroke quasi-zero stiffness vibration isolator using three-link mechanism. J. Sound Vib. **478**, 115344 (2020). https://doi.org/10.1016/j.jsv.2020.115344
16. Wang, K., Zhou, J., Chang, Y., Ouyang, H., Xu, D., Yang, Y.: A nonlinear ultra-low-frequency vibration isolator with dual quasi-zero-stiffness mechanism. Nonlinear Dyn. **101**, 755–773 (2020). https://doi.org/10.1007/s11071-020-05806-0
17. Bian, J., Jing, X.: Superior nonlinear passive damping characteristics of the bio-inspired limb-like or X-shaped structure. Mech. Syst. Signal Process. **125**, 21–51 (2019). https://doi.org/10.1016/j.ymssp.2018.02.014
18. Jiang, G., Jing, X., Guo, Y.: A novel bio-inspired multi-joint anti-vibration structure and its nonlinear HSLDS properties. Mech. Syst. Signal Process. **138**, 106552 (2020). https://doi.org/10.1016/j.ymssp.2019.106552
19. Niu, M.-Q., Chen, L.-Q.: Analysis of a bio-inspired vibration isolator with a compliant limb-like structure. Mech. Syst. Signal Process. **179**, 109348 (2022). https://doi.org/10.1016/j.ymssp.2022.109348
20. Yan, G., Qi, W.-H., Shi, J.-W., Yan, H., Zou, H.-X., Zhao, L.-C., Wu, Z.-Y., Fang, X.-Y., Li, X.-Y., Zhang, W.-M.: Bionic paw-inspired structure for vibration isolation with novel nonlinear compensation mechanism. J. Sound Vib. **525**, 116799 (2022). https://doi.org/10.1016/j.jsv.2022.116799
21. Yan, G., Zou, H.-X., Wang, S., Zhao, L.-C., Wu, Z.-Y., Zhang, W.-M.: Bio-inspired toe-like structure for low-frequency vibration isolation. Mech. Syst. Signal Process. **162**, 108010 (2022). https://doi.org/10.1016/j.ymssp.2021.108010
22. Ling, P., Miao, L., Zhang, W., Wu, C., Yan, B.: Cockroach-inspired structure for low-frequency vibration isolation. Mech. Syst. Signal Process. **171**, 108955 (2022). https://doi.org/10.1016/j.ymssp.2022.108955
23. Dai, H., Jing, X., Wang, Y., Yue, X., Yuan, J.: Post-capture vibration suppression of spacecraft via a bio-inspired isolation system. Mech. Syst. Signal Process. **105**, 214–240 (2018). https://doi.org/10.1016/j.ymssp.2017.12.015
24. Yan, G., Zou, H.-X., Wang, S., Zhao, L.-C., Wu, Z.-Y., Zhang, W.-M.: Bio-inspired vibration isolation: methodology and design. Appl. Mech. Rev. **73**, 020801 (2021). https://doi.org/10.1115/1.4049946
25. Hao, Z., Cao, Q., Wiercigroch, M.: Nonlinear dynamics of the quasi-zero-stiffness SD oscillator based upon the local and global bifurcation analyses. Nonlinear Dyn. **87**, 987–1014 (2017). https://doi.org/10.1007/s11071-016-3093-6
26. Zhao, F., Ji, J., Luo, Q., Cao, S., Chen, L., Du, W.: An improved quasi-zero stiffness isolator with two pairs of

oblique springs to increase isolation frequency band. Nonlinear Dyn. **104**, 349–365 (2021). https://doi.org/10.1007/s11071-021-06296-4
27. Zhao, F., Ji, J., Ye, K., Luo, Q.: An innovative quasi-zero stiffness isolator with three pairs of oblique springs. Int. J. Mech. Sci. **192**, 106093 (2021). https://doi.org/10.1016/j.ijmecsci.2020.106093
28. Yang, T., Cao, Q.: Time delay improves beneficial performance of a novel hybrid energy harvester. Nonlinear Dyn. **96**, 1511–1530 (2019). https://doi.org/10.1007/s11071-019-04868-z
29. Yang, T., Cao, Q.: Dynamics and performance evaluation of a novel tristable hybrid energy harvester for ultra-low level vibration resources. Int. J. Mech. Sci. **156**, 123–136 (2019). https://doi.org/10.1016/j.ijmecsci.2019.03.034
30. Mojahed, A., Moore, K., Bergman, L.A., Vakakis, A.F.: Strong geometric softening–hardening nonlinearities in an oscillator composed of linear stiffness and damping elements. Int. J. Non-Linear Mech. **107**, 94–111 (2018). https://doi.org/10.1016/j.ijnonlinmec.2018.09.004
31. Gatti, G., Ledezma-Ramirez, D.F., Brennan, M.J.: Performance of a shock isolator inspired by skeletal muscles. Int. J. Mech. Sci. **244**, 108066 (2023). https://doi.org/10.1016/j.ijmecsci.2022.108066
32. Gatti, G., Svelto, C.: Performance of a vibration isolator with sigmoidal force-deflection curve. J. Vibr. Control **29**(23–24), 5713–5724 (2023). https://doi.org/10.1177/10775463221139006
33. Zou, D., Liu, G., Rao, Z., Tan, T., Zhang, W., Liao, W.-H.: A device capable of customizing nonlinear forces for vibration energy harvesting, vibration isolation, and nonlinear energy sink. Mech. Syst. Signal Process. **147**, 107101 (2021). https://doi.org/10.1016/j.ymssp.2020.107101
34. Jing, X., Chai, Y., Chao, X., Bian, J.: In-situ adjustable nonlinear passive stiffness using X-shaped mechanisms. Mech. Syst. Signal Process. **170**, 108267 (2022). https://doi.org/10.1016/j.ymssp.2021.108267
35. Gatti, G.: An adjustable device to adaptively realise diverse nonlinear force-displacement characteristics. Mech. Syst. Signal Process. **180**, 109379 (2022). https://doi.org/10.1016/j.ymssp.2022.109379
36. Yan, G., Wu, Z.-Y., Wei, X.-S., Wang, S., Zou, H.-X., Zhao, L.-C., Qi, W.-H., Zhang, W.-M.: Nonlinear compensation method for quasi-zero stiffness vibration isolation. J. Sound Vib. **523**, 116743 (2022). https://doi.org/10.1016/j.jsv.2021.116743
37. Yang, H.T., Kwon, I.Y., Randall, C.J., Hansma, P.K., Ly, F.S.: Preliminary design, experiment, and numerical study of a prototype hydraulic bio-inspired damper. J. Sound Vib. **459**, 114845 (2019). https://doi.org/10.1016/j.jsv.2019.07.011
38. Gao, X., Teng, H.D.: Dynamics and nonlinear effects of a compact near-zero frequency vibration isolator with HSLD stiffness and fluid damping enhancement. Int. J. Non-Linear Mech. **128**, 103632 (2021). https://doi.org/10.1016/j.ijnonlinmec.2020.103632
39. Donmez, A., Cigeroglu, E., Ozgen, G.O.: An improved quasi-zero stiffness vibration isolation system utilizing dry friction damping. Nonlinear Dyn. **101**, 107–121 (2020). https://doi.org/10.1007/s11071-020-05685-5
40. Zhu, R., Marchesiello, S., Anastasio, D., Jiang, D., Fei, Q.: Nonlinear system identification of a double-well Duffing oscillator with position-dependent friction. Nonlinear Dyn. **108**, 2993–3008 (2022). https://doi.org/10.1007/s11071-022-07346-1
41. Marino, L., Cicirello, A.: Experimental investigation of a single-degree-of-freedom system with Coulomb friction. Nonlinear Dyn. **99**, 1781–1799 (2020). https://doi.org/10.1007/s11071-019-05443-2
42. Wojewoda, J., Stefanski, A., Wiercigroch, M., Kapitaniak, T.: Hysteretic effects of dry friction: modelling and experimental studies. Phil. Trans. R. Soc. A **366**, 747–765 (2008). https://doi.org/10.1098/rsta.2007.2125
43. Gatti, G.: Effect of parameters on the design of a suspension system with four oblique springs. Shock. Vib. **2021**, 5556088 (2021). https://doi.org/10.1155/2021/5556088
44. Meirovitch, L.: Principles and Techniques of Vibration, Prentice-Hall (1997).
45. Masri, S.F., Caughey, T.K.: A nonparametric identification technique for nonlinear dynamic problems. J. Appl. Mech. **46**, 433–447 (1979). https://doi.org/10.1115/1.3424568
46. Anastasio, D., Marchesiello, S.: Experimental characterization of friction in a negative stiffness nonlinear oscillator. Vibration **3**(2), 132–148 (2020). https://doi.org/10.3390/vibration3020011
47. Gatti, G., Svelto, C.: Exploiting nonlinearity for the design of linear oscillators: application to an inherently strong nonlinear X-shaped-spring suspension. Mech. Syst. Signal Process. **197**, 110362 (2023). https://doi.org/10.1016/j.ymssp.2023.110362
48. Brown, P., McPhee, J.: A continuous velocity-based friction model for dynamics and control with physically meaningful parameters. J. Comput. Nonlinear Dyn. **11**, 1–6 (2016). https://doi.org/10.1115/1.4033658
49. Anastasio, D., Marchesiello, S., Gatti, G., Gonçalves, P.J.P., Shaw, A.D., Brennan, M.J.: An investigation into model extrapolation and stability in the system identification of a nonlinear structure. Nonlinear Dyn. **111**, 17653–17665 (2023). https://doi.org/10.1007/s11071-023-08770-7
50. Wojewoda, J., Stefański, A., Wiercigroch, M., Kapitaniak, T.: Hysteretic effects of dry friction: modelling and experimental studies. Philos Trans A Math Phys Eng Sci. **366**, 1866 (2008). https://doi.org/10.1098/rsta.2007.2125
51. Conn, A.R., Gould, N.I.M., Toint, P.L.: Trust region methods. SIAM (2000). https://doi.org/10.1137/1.9780898719857